

## Appendix A.

1. Overview of study area .....	3
2. Data source.....	3
2.1. Forest Management Planning Inventory database.....	3
2.2. Human activity database .....	3
2.3. Land surface temperature database .....	3
3. Integration of remote sensing imagery and forest management planning inventory data .....	5
4. Spatial statistical analysis: cluster regions.....	5
4.1. Reasons for identifying the surrounding patches .....	5
4.2. Reasons for focusing on hot and cold spots .....	5
5. Spatial statistical analysis: GeogDetector model .....	6
6. Results.....	7
6.1. Geostatistical analysis of STUFC.....	7
6.2. Geostatistical analysis of urban forest stand structure.....	7
6.3. Geostatistical analysis of anthropogenic activity.....	8
7. Discussion .....	8
7.1 The restrictive factors for the integration research.....	8
References.....	9

Figure S1. Results for  $G_i^*$  at various search radii indicating the proportion of regions identified as hot and cold spots. .... 11

Figure S2. Change in STUFC, urban forest stand structure, and anthropogenic activity factors under local Getis–Ord  $G_i^*$  statistical distribution for 2004 (white boxes, no shadow) and 2014 (gray boxes, dense shadow): (a) Land surface temperature (LST), (b) forest patch area (PA), (c) dominant species (DS), (d) canopy density (CD), (e) stand age (SA), (f) shape index (ShI), (g) population density (PD), (h) impervious surface percent in 100 m radius (ISP100). The abscissa labels are as follows: entire study region (All), hot spots (HS), cold spots (CS), and nonsignificant areas (NS). PM, *Pinus massoniana*; AC, *Acacia*

*confusa*; EG, *Eucalyptus grandis*; CE, *Casuarina equisetifolia*; DL, *Dimocarpus longan*; OB, Other Broad-leaved trees. ....12

Figure S3. Locations of hot and cold spots of 14 factors in (a) 2004 and (b) 2014. PM: *Pinus massoniana*. AC: *Acacia confusa*, EG: *Eucalyptus grandis*, CE: *Casuarina equisetifolia*, DL: *Dimocarpus longan*..... 14

Figure S4. Influence of interactions in study areas in (a) 2004 and (b) 2014. .... 15

Figure S5. Influence of interactions in hotspot areas in (a) 2004 and (b) 2014..... 15

Figure S6. Influence of interactions in nonsignificant areas in (a) 2004 and (b) 2014. .... 15

## Appendix A.

### 1. Overview of Study Area

Jinjiang is one of the most developed counties in China. The total GDP of Jinjiang increased from RMB 48.387 billion in 2004 to RMB 149.286 billion in 2014, and the population increased over the same period from 1,029,000 to 1,108,000. Within a decade, Jinjiang's population increased by 17% to reach 63% in 2014. The soils are mostly laterite and red earth; urban forest coverage is at 39.76%.

### 2. Data Sources

#### 2.1. Forest Management Planning Inventory Database

The urban forest ground survey data used in this study were obtained from the 2004 and 2014 Jinjiang Forest Management Planning Inventories (FMPs). These data include the forest resource distribution drawings and compartment survey documents. The unique number of compartments is specified in the distribution maps. The compartment files record the serial number and attribute information. In future iterations of this study, the accuracy of each subcompartment attribute will be measured using both systematic sampling and stratified sampling. The overall volume sampling accuracy should be 90% or more and the reliability should be 95% or more [1]. In addition, the vector graphical data were used to calculate a patch shape index  $= P/\sqrt{4\pi A}$ , where  $P$  is the perimeter and  $A$  is the area. Our investigation will be conducted every 10 years and will yield valuable subcompartment data that are key to resource planning and environmental studies.

#### 2.2. Human Activity Database

With FMPI polygon serving as the basic unit, the spatiotemporal distributions of population density were mapped using the ArcGIS 10.0 space-analysis module functions for the kernel density tool and zonal statistics. Inversion via a double-channel algorithm was used to obtain urban LST raster data. For each patch, the average LST and population density were calculated. Initially, the 200 m compartment buffer circles for Jinjiang overlapped, so all compartments were connected. Therefore, we considered the 200 m buffer circle to be too large and calculated the impervious surface area ratio of the buffer circle area by using a 100 m radius from the edges of each patch [2].

#### 2.3. Land Surface Temperature Database

The Landsat remote sensing imagery maps are integrated with forest inventory data and converted to a uniform spatiotemporal scale [3,4]. The calculation was done under stable atmospheric conditions. The sixth wave band of the Landsat-5 data was used to estimate sensor brightness temperature, and the tenth wave band of the Landsat-8 TIRS data was used to estimate the sensor brightness temperature. The multispectral band of the Operational Land Imager and TM5 data were used to generate the normalized difference vegetation index (NDVI) for areas under investigation to improve the modified normalized difference water index and the normalized difference build-up index (which have also been used for emissivity estimates). The purpose of this study is to accurately classify surface features based on the decision tree model.

Currently, the algorithms proposed for Landsat 8 thermal infrared band land surface temperature (LST) retrieval include the Jimenez-Munoz single-channel algorithm [5], the mono-window algorithm by Qin et al. [6], the Rozenstein split-window algorithm [7], and the Jimenez-Munoz split-window algorithm [8]. For our purposes, we used the mono-window algorithm by Qin et al. [6] for single-channel retrieval.

The equations are

$$T_s = \frac{[a(1-C-D) + (b(1-C-D) + C + D)T_{sensor} - DT_a]}{C} \quad (1)$$

$$C = \tau\varepsilon \quad (2)$$

$$D = (1-\tau)[1 + (1-\varepsilon)\tau], \quad (3)$$

where  $\varepsilon$  is the land surface emissivity,  $\tau$  is the atmospheric transmissivity,  $T_{sensor}$  is the brightness temperature corresponding to the upper radiance,  $T_a$  is the atmospheric mean temperature, and  $a$ ,  $b$  are coefficients. By using the atmospheric radiation transmission software LOWTRAN for a simulation, Rozenstein et al. (2014) worked out the TIRS retrieval regression coefficients of different temperature ranges [7].

We used the mono-window algorithm to estimate atmospheric transmissivity and atmospheric mean temperature  $T_a$  of the TM data from Landsat-5 TM and the TIRS data from Landsat-8. To simulate the atmospheric parameters, the summer atmospheric profile data were input as MODTRAN atmospheric section data according to the geographic orientation and seasonal aspects of the experimental area.

### 2.3.1. Land Surface Emissivity

The following methods are currently being used to determine land surface emissivity: the difference value method, the temperature-independent spectral index (TISI) method, the NDVI threshold value method (NDVI-THM), and others [9]. To obtain  $\varepsilon$ , the classification and regression tree method (CART) was applied to classify land surface. Based on these results, land surface emissivity was estimated by using the emissivity estimation method adopted by Qin et al. [10].

### 2.3.2. Atmospheric Transmissivity

To retrieve land surface data, water vapor is a key factor affecting estimates of atmospheric transmissivity. The relation between atmospheric transmissivity and atmospheric water vapor content is determined by atmospheric simulation. In general, MODTRAN, 6S, and other atmospheric simulation software are used to simulate the relationship between atmospheric transmissivity and water-vapor content. Qin et al. [6] developed the Landsat 8 TIRS atmospheric transmissivity equation by using the atmospheric radiation transmission software LOWTRAN for simulations. By applying the atmospheric water vapor content to the equation, the calculated atmospheric transmissivity was 0.62.

### 2.3.3. Brightness Temperature

Using the conversion of image digital number into the satellite upper radiance data based on the calibration coefficient, the corresponding brightness temperature with the Planck function is obtained:

$$T_i = \frac{K_{i,2}}{\ln\left(1 + \frac{K_{i,1}}{I_i}\right)}, \quad (4)$$

where  $K_{i,1}$  and  $K_{i,2}$  are constants,  $K_{i,1} = \frac{2hc^2}{\lambda_i^5}$ ,  $K_{i,2} = \frac{hc}{K\lambda_i}$ ,  $h$  is Planck's constant

( $\sim 6.62606896$ ),  $c$  is the speed of light ( $\sim 2.99792 \times 10^8$  m/s),  $k$  is the Boltzmann constant ( $\sim 1.3806505 \times 10^{-23}$  J/K), and  $\lambda_i$  is the central wavelength in channel  $i$ .

### 3. Integration of Remote Sensing Imagery and Forest Management Planning Inventory Data

We calibrated the sample-plot investigation data and the topographic map. During calibration, the topographic map, the texture properties of TM images, and Google Earth provided the basis for the validation of land-use type and key registration points (e.g., mountaintops). According to our study of relatively-low-resolution TM images, land-use classification based on a mean value rather than a single image cell does not impact the fusion calibration of the overall data.

Concurrently, the matched spatial data (i.e., multiple ecological factors, population, and temperature,) were converted to the WGS 1984 UTM (50N) coordinate system. For calibration, the ArcGIS 10.0 geo-referencing function was used. The result of this integration formed our new attribute database.

### 4. Spatial Statistical Analysis: Cluster Regions

#### 4.1. Reasons for Identifying the Surrounding Patches

The local Getis–Ord  $G_i^*$  statistics were calculated with 500–3500 m threshold distances and 250 m intervals (Figure S1). With the larger distance, we found that the minimum number of significant neighboring patches exceeded eight when the distance reached the 2250 m radius threshold in 2004, and this condition was satisfied by the 2000 m radius threshold in 2014. In addition, the total area of hot and cold spots increased at the beginning, and reached stable conditions at the 2250 m threshold (rate of increase 2.35% in 2004 and 0.54% in 2014). The proportion of total hot and cold spot area was 82.94% in 2004 and 62.55% in 2014. Therefore, the modeling of spatial positioning of hot-spot clusters (high value next to high value) and cold-spot clusters (low value next to low value) under the specific threshold distance scale (2,250 m) of urban STUFC was done by using Local Getis–Ord  $G_i^*$  statistics.

#### 4.2 Reasons for Focusing on Hot and Cold Spots

We further considered that the global Moran's I exponent, on the basis of the urban forest polygon data, verified that these spatial correlations indicated clustering. The capacity to evaluate spatial linkage and spatial change by using spatial statistics has enhanced the evaluation of authentic landscape heterogeneity in key areas of the urban ecological system. The hot- and cold-spot data generated by using local spatial statistics can serve as a reference for future spatial monitoring and can also be used to verify the accuracy of large-scale aerial remote sensing imagery. After understanding the mechanisms driving STUFC hot-spot areas, it will be important to include corresponding intervening measures that ensure the rational allocation of urban forest spatial resources to reduce LST.

Almost all spatial data are subject to spatial dependence and spatial autocorrelation. To this end, the spatial autocorrelation statistical index mainly consist of the global exponential indexes (including Moran's I, Geary's C, and Global G) and a local exponential index (including Moran's I, which is also known as LISA, and Getis–Ord  $G_i^*$ ). Specifically, the spatial stability of STUFC hot and cold spots leads to the assumption that the application of a spatial autocorrelation statistical index is accurate, i.e., it is assumed that the STUFC distribution is influenced by an ecological process that continuously changes with the spatial weight matrix and may be quantified by using the spatial autocorrelation statistical index. Global Moran's I uses the overall space of the whole urban forest patches as the statistical magnitude, which is the most commonly used index for measuring spatial correlation. Moran's I may indicate the presence of clustering, but it is not competent to detect hot- and cold-spot clustering. Only the local exponential index can recognize the existence of hot- and cold-spot clusters in relation to STUFC without the specific spatial location data, which can be obtained by using local Moran's I (also named LISA) or Getis–Ord  $G_i^*$ . Moran's I may be used to detect the abnormal spatial values in LST compartments or to detect the discrepancies

between LST compartments. The results achieved using this method, however, cannot be deemed conclusive regarding the specific spatial locations of hot and cold spots. Without considering neighboring forest stands, the local Getis–Ord  $G_i^*$  only adopts the standard distance measurement to identify spatial position when detecting LST hot- and cold-spot clusters in forest patches. From 2002 to 2013 in the United States, Potter et al. studied the spatial structure mode relating to plant invasion, plant death from plant diseases and insects, and urban forest fire frequency [11]. They verified that the identification of the spatial location of hot- and cold-spot clustering using the combination of global Moran’s I and local  $G_i^*(d)$  allows researchers to measure statistical significance at specific levels, which is a rigorous measurement method.

## 5. Spatial Statistical Analysis: GeogDetector Model

The GeogDetector software has been used to map environmental factors in relation to neural tube defects [12], geographic mortality in children younger than five years old, and fluoroquinolone residues in the soil based on the consistency of variable spatial patterns [13]. GeogDetector has four components to map, model, and analyze variable grid data integrated with a geographical interface. In this study, two components we used:

### (1) Factor detector

This detector quantifies the impact of a factor  $D$  on the observed spatial pattern of ecological-factor residues by using  $q$  value (Power of determinant,  $PD$ ), the dispersion variance ( $\sigma_{D,p}^2$ ) of pooled data of the entire region, and the sum of stratified dispersion variance ( $\sigma_{D,z}^2$ ). Therefore, the  $q$  value for factor  $D$  can be expressed by using

$$q = 1 - \frac{\sum_{p=1}^m n\sigma_{D,p}^2}{N\sigma_{D,z}^2}, \quad (5)$$

where  $q$  represents the determinant power of each impact factor, the hypothesis  $D$  is a potential impact factor,  $n$  is the number of samples in the sub-region affecting factor  $D$ ,  $N$  is the number of samples in the entire region,  $m$  is the number of impact factors,  $\sigma_{D,p}^2$  is the variance of the variable in sub-region  $D$ , and  $\sigma_{D,z}^2$  represents the discrete variance across the study area. Assuming  $\sigma_{D,z}^2 \neq 0$ , the model is established. The quantity  $q$  varies over the interval  $[0, 1]$ . A large  $q$  indicates that the explanatory variable factor has a strong influence on the explained variable.

### (2) Interaction detector

This detector quantifies the combined effect of two factors  $X_1$  and  $X_2$ ; for example, by overlaying geographical layers  $X_1$  and  $X_2$  in a GIS environment to form a new layer  $X_1 \cap X_2$ . With the  $q$  values for layers  $X_1$ ,  $X_2$  and  $X_1 \cap X_2$ , the interaction detector can deal with the interesting issue of whether two factors acting together have a stronger or weaker effect on LST residues than when they act separately.

$$\begin{aligned}
& \text{Weaken, nolinear—} : q(X_1 \cap X_2) < \text{Min}(q(X_1), q(X_2)) \\
& \text{Weaken, u ni—} : \text{Min}(q(X_1), q(X_2)) < q(X_1 \cap X_2) < \text{Max}(q(X_1), q(X_2)) \\
& \text{Enhance, bi—} : q(X_1 \cap X_2) > \text{Max}(q(X_1), q(X_2)) \\
& \text{Independent—} : q(X_1 \cap X_2) = q(X_1) + q(X_2) \\
& \text{Enhance, nonlinear—} : q(X_1 \cap X_2) > q(X_1) + q(X_2)
\end{aligned} \tag{6}$$

## 6. Results

### 6.1. Geostatistical Analysis of STUFC

By using the global Moran's I index, our analysis of STUFC showed spatial autocorrelation, and its spatial clustering decreased (Moran's index was 0.476 in 2004; 0.178 in 2014; Table 2). We analyzed the temporal and spatial variations in the STUFC. Based on a distance to neighboring forest patch of 2250 m, the local Getis-Ord  $G_i^*$  statistics indicated that the number of hot spot patches increased (1543 in 2004 and 2444 in 2014), as did the number of cold spots, although to a lesser extent (1059 in 2004 and 1458 in 2014). In addition, nonsignificant clustering areas increased dramatically (698 in 2004 and 2,061 in 2014). The total area of statistically significant hot and cold spots was 2847.18 ha (both in 2004 and 2014). Hot and cold spots also exhibited the largest differences in the degrees of spatial clustering (Figure 5). We used a box plot (Figure S2) to compare the STUFC for four areas (total area, hot spots, cold spots, and nonsignificant clustering areas). The average STUFC in cold spots (-0.091 in 2004 and -0.133 in 2014) was significantly less than that in hot spots (0.042 in 2004 and 0.002 in 2014) and non-clustering areas (0.001 in 2004 and -0.052 in 2014).

With respect to cluster position, the locations of hot and cold spots were similar in 2004 and 2014. The hot spots were distributed mainly in the northwestern and southeastern corners of the city, and the cold spots were distributed mainly in the hilly areas of the north, central, and east-central regions.

### 6.1 6.2. Geostatistical Analysis of Urban Forest Stand Structure

To clarify the mechanism of STUFC influence on hot and cold spots between 2004 and 2014, we need to know the urban forest stand structure dynamics. We considered the following characteristics: patch area, canopy density, stand age, shape index, and dominant species.

The total forest area of hot (decreased 1336.338 ha) and cold (decreased 1611.518 ha) spots decreased by 2947.846 ha over these 10 years. Nonsignificant (accounted for 18.04% and 37.45% of the total area in 2004 and 2014, respectively) areas increased by 1616.589 ha. The transfer matrix shows that, in 2004 and 2014, the area of urban forest undergoing conversion from hot spots to cold spots and non-clustering areas was 2035.970 ha. Within this area, 1393.680 ha of cold and hot spots transitioned into nonsignificant areas. The conversion between cold and hot spots was less; only 232.404 ha. The average of canopy density (increased by 0.093 and 0.179 in hot and cold spots, respectively) and stand age (increased by 4.919 years and 5.926 years in hot and cold spots, respectively) both increased between 2004 and 2014. The shape index increased 0.096 in hot spots, but decreased 0.372 in cold spots. Meanwhile, these five dominant tree species in hot spots accounted for more than 80% of the forest stands (81.86% in 2004 and 83.18% in 2014), whereas the proportion of the five most-dominant tree species in cold spots decreased from 79.28% in 2004 to 54.58% in 2014. These results indicate that the composition of tree species in cold spots became more complex, which signals enhanced diversity.

### 6.2 6.3. Geostatistical Analysis of Anthropogenic Activity

The overall spatial clustering degree of population density tended to decrease (global Moran's  $I = 0.731$ ,  $z$ -score = 199.072 in 2004; global Moran's  $I = 0.642$ ,  $z$ -score = 269.293 in 2014). Local Getis-Ord  $G_i^*$  statistics show that, in hot spots, the population density increased from  $1113.0 \pm 360.7$  people  $ha^{-1}$  in 2004 to  $1257.5 \pm 586.0$  people  $ha^{-1}$  in 2014. In contrast, the population density in cold spots decreased from  $990.1 \pm 561.0$  to  $892.7 \pm 439.5$  people  $ha^{-1}$ . The population density in nonsignificant areas was  $1330.0 \pm 606.3$  people  $ha^{-1}$  in 2004 and  $1379.0 \pm 638.0$  people  $ha^{-1}$  in 2014. From 2004 to 2014, the total impervious surface area increased from 38.05% to 51.42%. The average within a 100 m radius increased 14.95% and 12.08% in hot and cold spots, respectively (Figure 6).

## 7. Discussion

### 7.1. The Restrictive Factors for the Integration Research

Recently, research into the LST of forest is mainly conducted based on the sample plot scale obtained by using long-term sample-plot survey data and the landscape scale of remote sensing imagery. However, two challenges remain: (1) a lack of reliable vegetation index, and (2) issues related to the integration of the sample-plot data and landscape-scale data.

Specifically, the vegetation index (i.e., NDVI), which is based on the interpretation of remote sensing imagery, is not verifiable in terms of eco-environmental significance. Because of the sophisticated ecological factors and interactions that affect the urban environment, the features of LST of forest can hardly be fully described by only one vegetation index. Various issues relating to the statistics and algorithms between LST and vegetation index remain unsettled. In addition, remote sensing imagery is a pixel-based method, and the LST value is captured by the image as a mean value rather than as a sampling-point value. Previous land surface investigations have used survey data from limited sampling points, which fails to provide the true attribute data on a regional scale.

Although remote sensing imagery, temperature and vegetation indices, energy-balance models, and statistical analyses have been used in many studies to characterize the spatial distribution of LST on regional scales, few studies look at the complex changes in function and structure in forest areas [14]. The lack of available data on regional scale limits our efforts to quantify LST spatial heterogeneity and its causes in these areas. Many scholars agree that analyses relying on remote sensing imagery alone suffer from several significant problems. For example, Tooke et al. reported that traditional classification based on remote sensing imagery cannot explain mixed pixels [15]. Specifically, spectral reflectance characteristics are not used in this method to classify and quantify vegetation. Moreover, the heterogeneity of urban forest is difficult to characterize on a local scale by using single-image pixels. Geometric variability is caused by the intensification of high-resolution images and, coupled with the field of view and illumination effect, accurate extraction of consistent vegetation data on different spatiotemporal scales becomes highly unlikely [16]. Furthermore, resolution and classification errors can also impact the accuracy of mapping and landscape patterns. Thus, the causes of LST pattern changes must be determined by coupling LST information from remote sensing imagery with a multi-source database on a unified scale.

Forest management planning inventories not only provide detailed information on multiple ecological factors affecting forest stands, but also can be used to validate remote sensing interpretations and quantitative analyses [17]. Although the integration of multiple data sources can lead to uncertainty, this uncertainty can be significantly reduced by calibrating the size and format of all data sources and by ensuring the accuracy of the data [18]. Forest-resource planning and design data comprise a set of land surface investigation data on the whole-forest regional scale, and these data can be used to supplement data

obtained from remote sensing imagery.

## 7.2. Enlightenment

In brief, the decreasing spatial clustering trend in STUFC and population density from 2004 to 2014 shows an expanding influence of anthropogenic activity on the spatial range of urban forest. Meanwhile, the consistency of the spatiotemporal distribution patterns for anthropogenic activity (PD and ISP100) and for STUFC suggests that anthropogenic activity affects the spatiotemporal distribution pattern of STUFC through land-use change, anthropogenic heat emissions, and environmental pollution [20]. Simultaneously, anthropogenic activity facilitates the spatial heterogeneity of STUFC because, when connected to construction land, and the STUFC does not exhibit spatial clustering. Urban sprawl leads to more and more urban forest located in densely populated urban environments. Anthropogenic disturbance is long-term and continuous. Therefore, comparing the changes in the global Moran's I and local  $G_i^*$  index in the different periods of urbanization would help to clarify the relationship between urban forest landscape pattern and process. Furthermore, it is an important directive function to optimize the regional urban forest cold-island effect. Using a local  $G_i^*$  method to spatially identify the specific location of LST cold spots in urban forests is a key step in understanding the ecological process of atypical spatial patterns. Based on the detection regions, we used the Geodetector model to clarify the spatial relationship between multiple impact factors including human activity factors and STUFC in cold spots.

Although the forest area factor has less influence on the STUFC in the cold spots in 2014, whether the size of the forest area is important for the cooling effect of urban forests is not simple to determine because the influence of this factor on STUFC is closely related to the degree of forest fragmentation and connectivity at a specific time and place. More importantly, the interactive effect with other factors is greater than the effect of the forest area factor itself.

## Appendix B.

### References

1. Lei, X.D.; Tang, M.P.; Lu, Y.C.; Hong, L.X.; Tian, D.L. Forest inventory in China: Status and challenges. *International Forestry Review* **2009**, *11*, 52-63.
2. Pincetl, S.; Gillespie, T.W.; Pataki, D.E.; Saatchi, S.; Saphores, J. Urban tree planting programs, function or fashion? Los angeles and urban tree planting campaigns. *GeoJournal* **2013**, *78*, 475-493.
3. Hilker, T.; Wulder, M.A.; Coops, N.C.; Linke, J.; McDermid, G.; Masek, J.G.; Gao, F.; White, J.C. A new data fusion model for high spatial- and temporal-resolution mapping of forest disturbance based on landsat and modis. *Remote Sensing of Environment* **2009**, *113*, 1613-1627.
4. Styers, D.M.; Chappelka, A.H.; Marzen, L.J.; Somers, G.L. Scale matters: Indicators of ecological health along the urban-rural interface near columbus, georgia. *Ecological Indicators* **2010**, *10*, 224-233.
5. Jimenezmunoz, J.C.; Cristobal, J.; Sobrino, J.A.; Soria, G.; Ninyerola, M.; Pons, X. Revision of the single-channel algorithm for land surface temperature retrieval from landsat thermal-infrared data. *IEEE Transactions on Geoscience and Remote Sensing* **2009**, *47*, 339-349.
6. Qin, Z.; Karnieli, A.; Berliner, P.R. A mono-window algorithm for retrieving land surface temperature from landsat tm data and its application to the israel-egypt border region. *Int J Remote Sens* **2001**, *22*, 3719-3746.
7. Rozenstein, O.; Qin, Z.; Derimian, Y.; Karnieli, A. Derivation of land surface

- temperature for landsat-8 tirs using a split window algorithm. *Sensors* **2014**, *14*, 5768-5780.
8. Jimenezmunoz, J.C.; Sobrino, J.A.; Skokovic, D.; Mattar, C.; Cristobal, J. Land surface temperature retrieval methods from landsat-8 thermal infrared sensor data. *IEEE Geoscience and Remote Sensing Letters* **2014**, *11*, 1840-1843.
  9. Fu, P.; Weng, Q. Consistent land surface temperature data generation from irregularly spaced landsat imagery. *Remote Sensing of Environment* **2016**, *184*, 175-187.
  10. Jia, Q.Z.L.W.X.B.C.Z.L. The estimation of land surface emissivity for landsat tm6. *Remote Sensing for Land & Resources* **2011**, *16*.
  11. Potter, K.M.; Koch, F.H.; Oswalt, C.M.; Iannone, B.V. Data, data everywhere: Detecting spatial patterns in fine-scale ecological information collected across a continent. *Landscape Ecology* **2016**, *31*, 67-84.
  12. Wang, J.F.; Li, X.H.; Christakos, G.; Liao, Y.L.; Zhang, T.; Gu, X.; Zheng, X.Y. Geographical detectors-based health risk assessment and its application in the neural tube defects study of the heshun region, China. *International Journal of Geographical Information Science* **2010**, *24*, 107-127.
  13. Xu, C. Spatio-temporal pattern and risk factor analysis of hand, foot and mouth disease associated with under-five morbidity in the beijing–tianjin–hebei region of China. *International Journal of Environmental Research and Public Health* **2017**, *14*, 416.
  14. Ren, Y.; Deng, L.Y.; Zuo, S.D.; Song, X.D.; Liao, Y.L.; Xu, C.D.; Chen, Q.; Hua, L.Z.; Li, Z.W. Quantifying the influences of various ecological factors on land surface temperature of urban forests *Environmental Pollution* **2016**, *216*, 519-529.
  15. Tooke, T.R.; Coops, N.C.; Goodwin, N.R.; Voogt, J.A. Extracting urban vegetation characteristics using spectral mixture analysis and decision tree classifications. *Remote Sensing of Environment* **2009**, *113*, 398-407.
  16. Chen, X.L.; Zhao, H.M.; Li, P.X.; Yin, Z.Y. Remote sensing image-based analysis of the relationship between urban heat island and land use/cover changes. *Remote Sensing of Environment* **2006**, *104*, 133-146.
  17. Ren, Y.; Deng, L.; Zuo, S.; Luo, Y.; Shao, G.; Wei, X.; Hua, L.; Yang, Y. Geographical modeling of spatial interaction between human activity and forest connectivity in an urban landscape of southeast China. *Landscape Ecology* **2014**, *29*, 1741-1758.
  18. Li, J.; Song, C.; Cao, L.; Zhu, F.; Meng, X.; Wu, J. Impacts of landscape structure on surface urban heat islands: A case study of Shanghai, China. *Remote Sensing of Environment* **2011**, *115*, 3249-3263.

Appendix C.

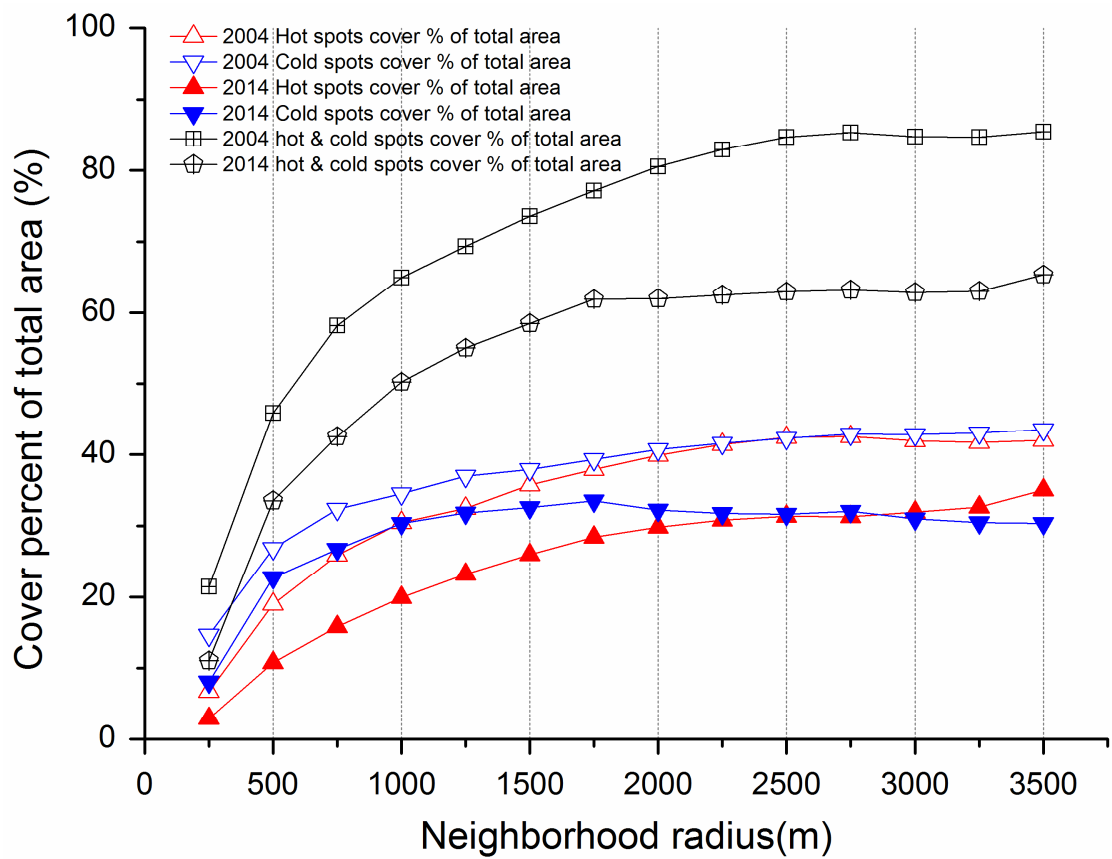
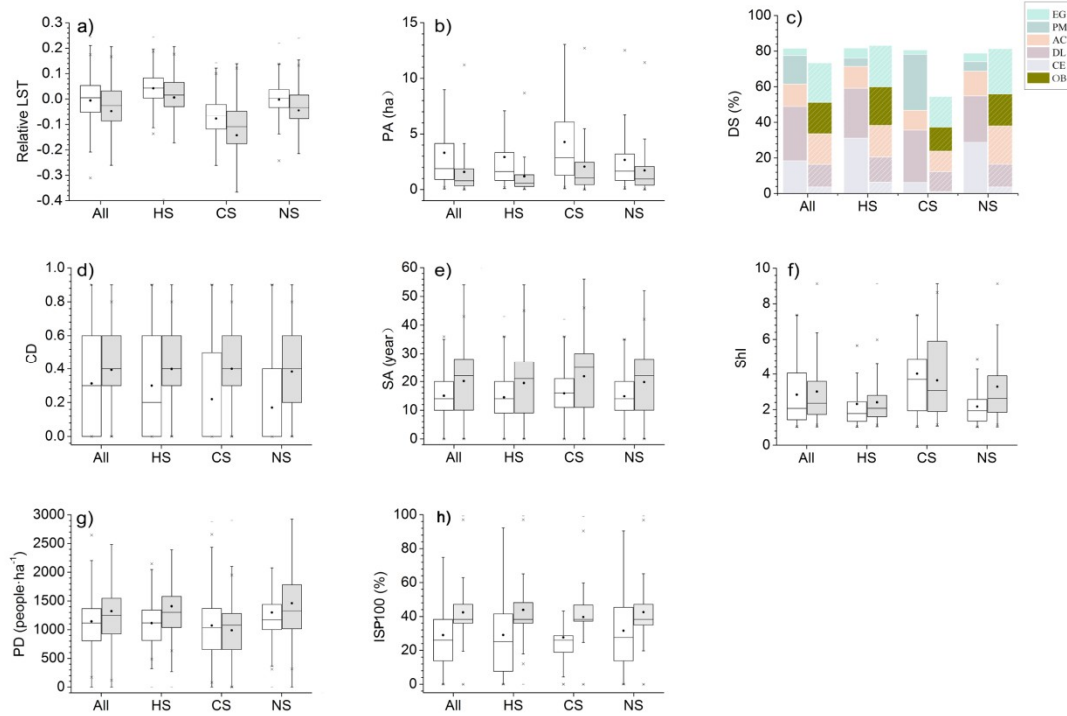


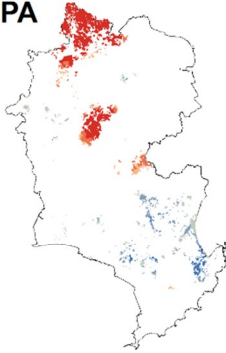
Figure S1. Results for  $G_i^*$  at various search radii indicating the proportion of regions identified as hot and cold spots.



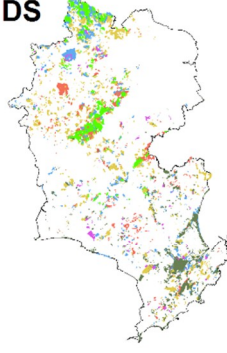
**Figure S2.** Change in STUFC, urban forest stand structure, and anthropogenic activity factors under local Getis-Ord  $G_i^*$  statistical distribution for 2004 (white boxes, no shadow) and 2014 (gray boxes, dense shadow): (a) Land surface temperature (LST), (b) forest patch area (PA), (c) dominant species (DS), (d) canopy density (CD), (e) stand age (SA), (f) shape index (ShI), (g) population density (PD), (h) impervious surface percent in 100 m radius (ISP100). The abscissa labels are as follows: entire study region (All), hot spots (HS), cold spots (CS), and nonsignificant areas (NS). PM *Pinus massoniana*. AC, *Acacia confusa*; EG, *Eucalyptus grandis*; CE, *Casuarina equisetifolia*; DL, *Dimocarpus longan*; OB, Other Broad-leaved trees.

a) 2004

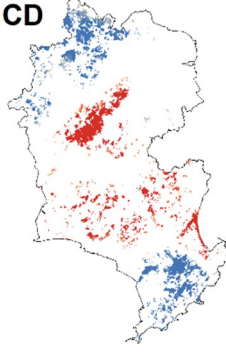
PA



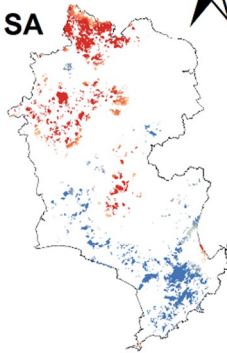
DS



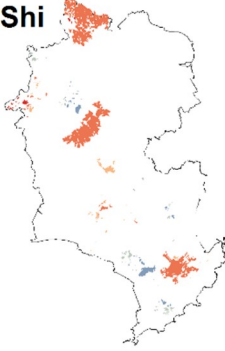
CD



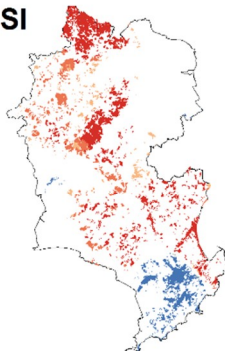
SA



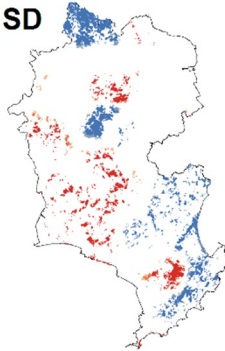
Shi



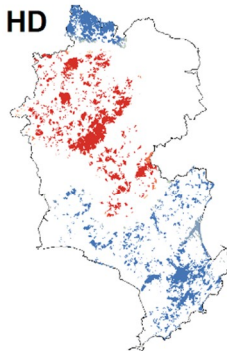
SI



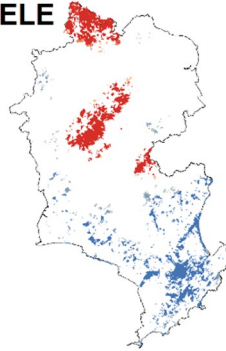
SD



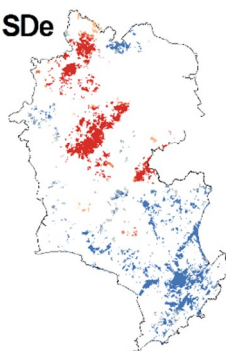
HD



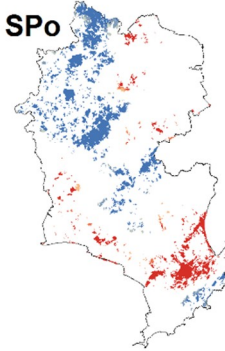
ELE



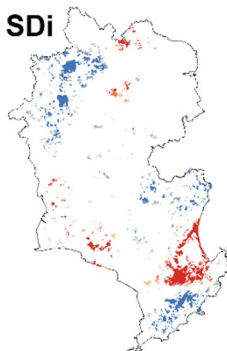
SDe



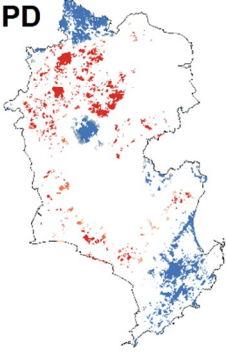
SPo



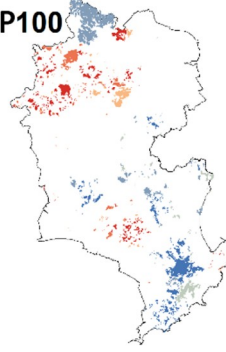
SDi



PD



ISP100



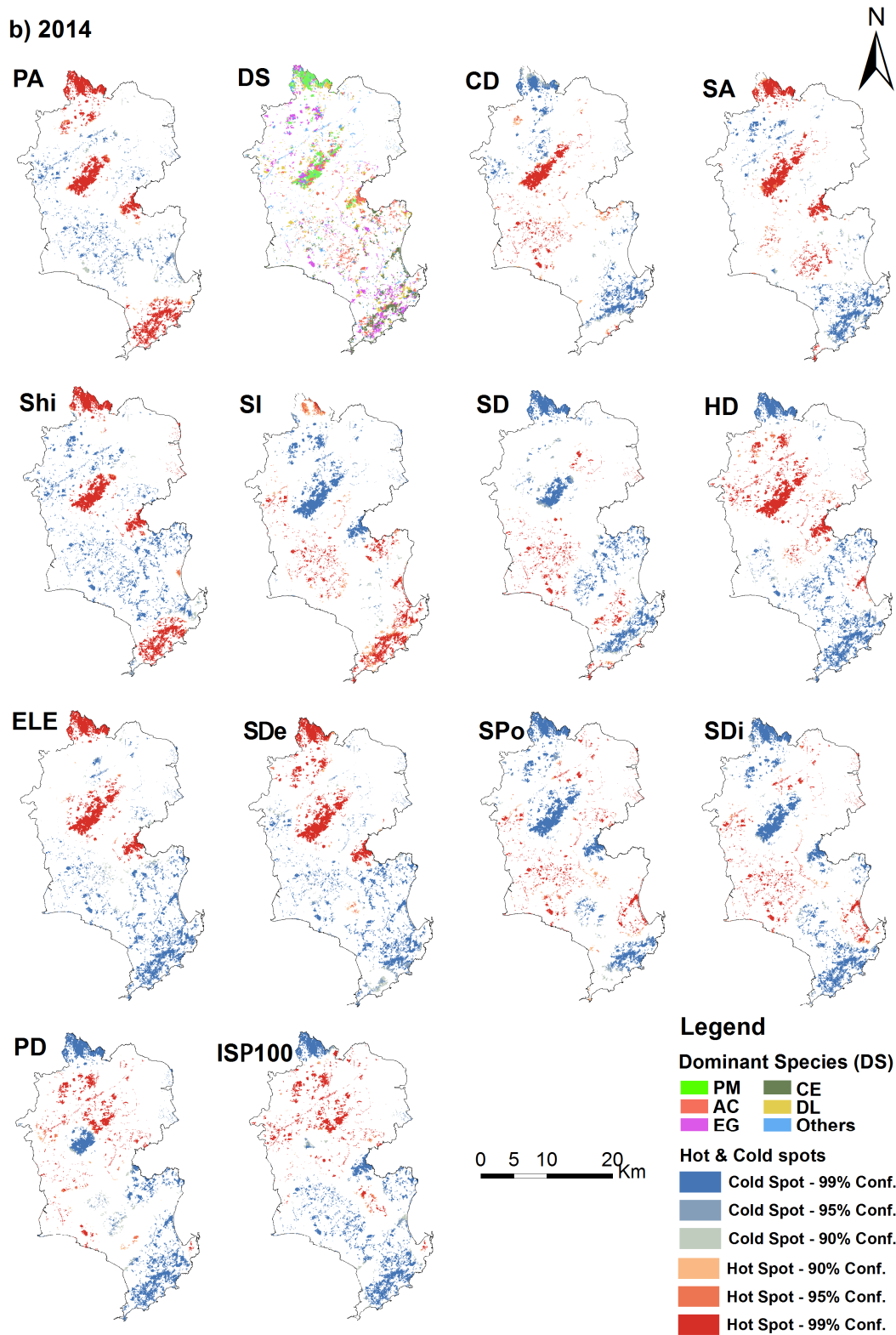


**Figure S3.** Locations of hot and cold spots of 14 factors in (a) 2004 and (b) 2014. PM: *Pinus massoniana*. AC: *Acacia confusa*, EG: *Eucalyptus grandis*, CE: *Casuarina equisetifolia*, DL: *Dimocarpus longan*.

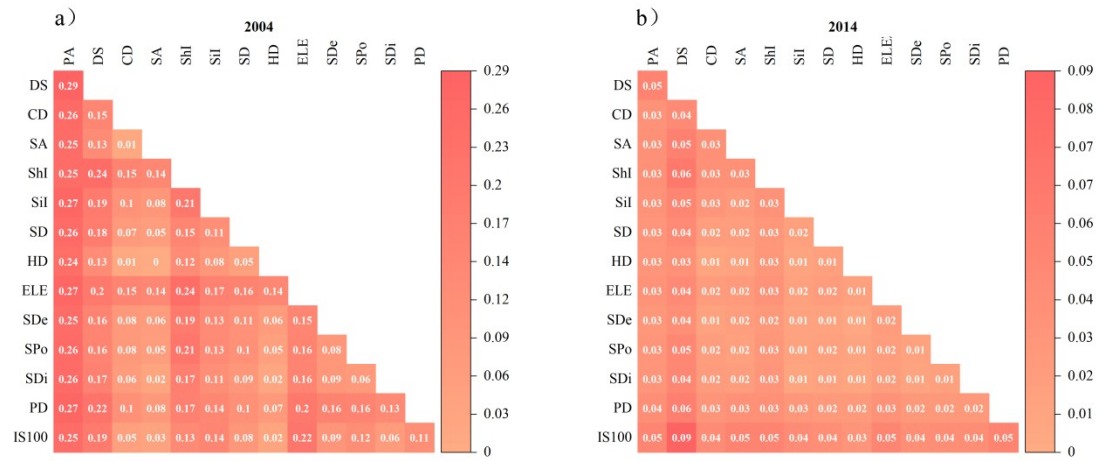


Figure S4. Influence of interactions in study areas in (a) 2004 and (b) 2014.

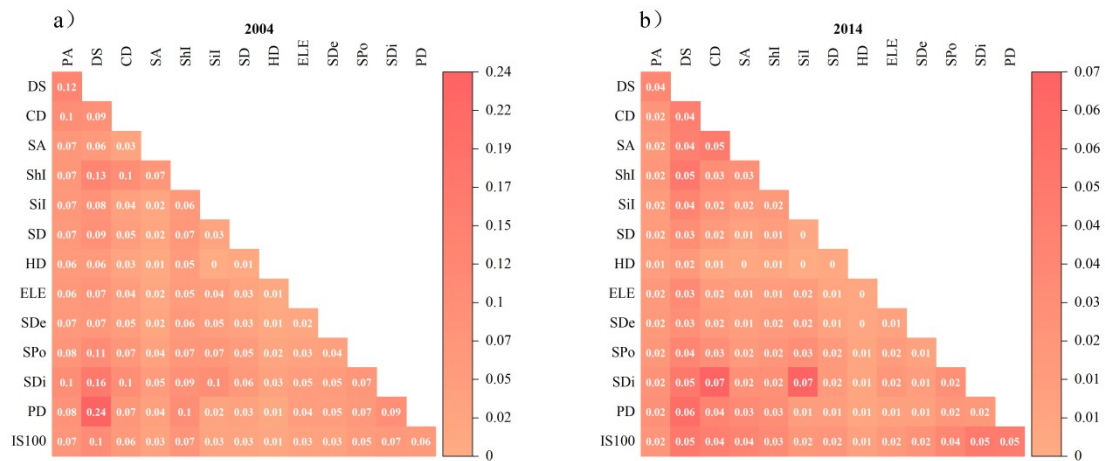


Figure S5. Influence of interactions in hotspot areas in (a) 2004 and (b) 2014.

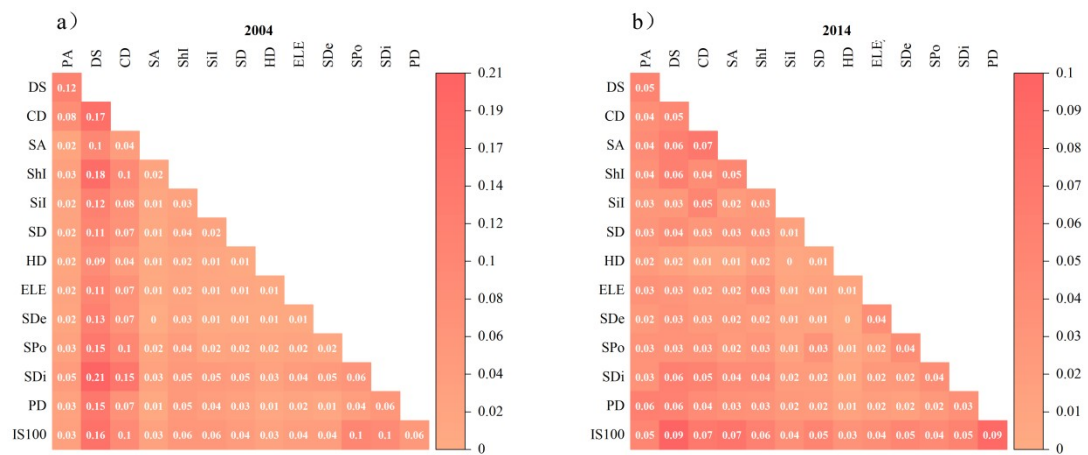


Figure S6. Influence of interactions in nonsignificant areas in (a) 2004 and (b) 2014.